# Calibrating the wings of the *Chandra* PSF

T. J. Gaetz, R. J. Edgar, D. Jerius, P. Zhao, and R. K. Smith,

Harvard-Smithsonian Center for Astrophysics, Cambridge, MA 02138, USA

## ABSTRACT

We discuss the calibration of the wings of the Chandra point spread function. In order to achieve high resolution imaging, the X-ray mirror surfaces must be extremely smooth in order to suppress the effects of scattering from microroughness. In the Chandra program, surfaces with only 1.3–3 Å roughness were achieved over more than 90% of the mirror length. We describe the current state of the calibration of the Chandra PSF wings, incorporating the results of a deep observation of the X-ray source Her X-1. The galactic Hydrogen column density ($N_H$) to Her X-1 is small, reducing the amplitude of any astrophysical dust scattering halo which would contaminate the mirror scattering wings. The X-ray data clearly show the shadows of the mirror support struts, confirming that the observed halo is predominantly due to mirror scattering. The extreme brightness of the source allows the energy dependence of the PSF wings to be probed with good statistics. The deep observation (heavily piled up in the core) is combined with a zero order gratings observation (unpiled in the core) to construct an energy-dependent profile.

**Keywords:** X-ray optics, PSF, scattering wings, Chandra

## 1. INTRODUCTION

The *Chandra* X-ray Observatory is the highest resolution X-ray telescope ever built, achieving subarcsecond imaging. In order to exploit fully the capabilities of the telescope, it is necessary to understand the energy-dependent point spread function (PSF) profile over its full angular range. The PSF of the *Chandra* High Resolution Mirror Assembly (HRMA) includes contributions ranging from nearly specular reflection from low frequency figure errors (the "core" of the PSF) to scattered photons reflecting/diffracting off of surface microroughness on the optics. The scattered photons form a faint diffuse halo extending to large angles. The on-axis, azimuthally-averaged scattering halo is energy dependent, falling approximately as a powerlaw ($\theta^{-\gamma}$), where $\theta$ is the angle from the center of the specular image, and $\gamma \sim 2$.

Extremely smooth mirror surfaces are required in order to attain such high performance. The ground metrology of the mirrors established that the 1 to 1000 mm$^{-1}$ surface roughness is ∼1.5–3 Å for the middle 770 (of 832) mm of each optic [1]. The ends of the optics are rougher, and the mean surface roughness including the ends is ∼ 2–6 Å. Ground measurements of the X-ray scattering wings were consistent with these values. Much effort at the ground testing was aimed at calibrating a high fidelity raytrace model for the HRMA performance. However, deficiencies in the scattering model and systematics in the ground testing (*e.g.*, uneven illumination of the rougher ends of the optics) led to substantial uncertainties in the PSF wings.

Detailed knowledge of this mirror scattering halo as a function of energy and radius is needed for interpretation of observations with faint structure adjacent to bright sources. Examples include:

- X-ray scattering halos from cosmic dust along the line of sight
- extracting faint sources adjacent to bright sources
- faint structure (*e.g.*, cosmic ray precursors) ahead of shocks in supernova remnants

Send correspondence to TJG; E-mail: gaetz@head-cfa.harvard.edu



This paper will be published in *X-ray and Gamma-Ray Instrumentation for Astronomy XIII*, Proceedings of SPIE Vol. 5165, and is made available as an electronic reprint with permission of SPIE. 

In order to better understand the PSF and the wings as a function of energy, we examine on-orbit data using ACIS as the detector. Because of detector pileup issues, ACIS has a relatively limited dynamical range. The detector evaluates event positions and energies based on the charge detected within $3 \times 3$ pixel islands. If more than one event contributes significant charge to an island within the frame accumulation time (typically 3.2 seconds), the energy of the detected event is perturbed; with severe pileup, the event is no longer detected as a valid X-ray event. This presents formidable problems for studying the PSF. The core of the *Chandra* PSF is very narrow (subpixel) and requires very faint sources in order to avoid pileup. The far wings are very faint compared to the core: a very bright source is needed in order to see the wings with good statistics above the detector background, resulting in heavy pileup in the core and inner wings. Because of this severe pileup, normalizing a wings observation is problematic because of difficulties in assessing the true source rate. In principle, the full radial PSF could be built up by overlapping data for varying degrees of pileup, which is the approach tried in this paper.

When using astronomical sources, great care is also needed to avoid building astrophysics into the calibration. For example, any intervening dust column will scatter X-rays and produce an X-ray dust scattering halo. This is most important at low energies; the total dust-scattered power scales roughly as $E^{-2}$, but at fixed angle, the amplitude scales very roughly as $E^{-1}$. In order to minimize the effects of dust halos, it is necessary to use sources with as low an $N_H$ column as possible. Another potential contaminant is diffuse emission such as emission from the galaxy hosting an active galactic nucleus (AGN). Indeed, 3C273, initially used in this study, showed indications of structure at scales of several arcseconds; it was thus rejected. Consequently, the most promising candidates are stellar sources and compact objects.

In this paper, we present the results of the first attempts to produce a *Chandra* radial PSF, as a function of energy, extending from the core of the PSF out into the far wings. Because astrophysical complications tend to broaden the profile (extended emission, cosmic dust halo, *etc.*) the resulting profiles tend to be overestimates of the PSF. Note, however, that this work is primarily concerned with finding the scaling for the near wings and far wings of the PSF; the treatment of the core of the PSF is only approximate.

## 2. OBSERVATIONS

In order to calibrate the far wings of the PSF, Her X-1 was observed. Her X-1 was selected because it is a very bright source (in its high state) at high galactic latitude ($b = 37.52$), with low extinction ($E[B-V] < 0.05$; see [2]). The total galactic column in that direction is $N_{\rm H} \sim 1.8 \times 10^{20}{\rm cm}^{-2}$ [3]; the total X-ray cosmic dust scattering halo is likely $\lesssim 1.5\%$ [4]. Her X-1 was observed by *Chandra* for 50 ks on July 1-2, 2002, imaged on a corner of the ACIS S3 chip with the detector translated to place the image $\sim 45''$ from the optical axis. Although the source is somewhat off-axis, this does not significantly affect the far wings — $0.75'$ is much smaller than the mean graze angle of the smallest mirror pair ($\sim 27'$). The ACIS I2, I3, and S2 chips were also on to provide additional coverage. The nominal ACIS frame time was 3.1 seconds. The Very Faint (VF) Timed Exposure (TE) mode was used, although the current study does not apply VF filtering. The radiation environment was quiescent (no flares) and the background, evaluated for 11–13 keV, was 4.83% higher than that for the appropriate blank sky background dataset (acis7sD20001201bkgrndN002.fits).

**Table 1.** Summary of Observations

| | obsid | Object | Exposure | Frame Time | $\theta$ | $N_H$( cm$^{-2}$) |
|---|---|---|---|---|---|---|
| Wings | 3662 | Her X-1 high state | 50 ks | 3.1 s | $45''$ | $1.8 \times 10^{20}$ |
| Core | 2749 | Her X-1 low state (zero order) | 50 ks | 3.2 s | $8''$ | $1.8 \times 10^{20}$ |

Because the central part of the profile is heavily piled up, the profile inside $\sim 10''$ cannot be determined from this observation. There have been no calibration observations with ACIS specifically targeting the PSF core, so we searched for serendipitous data which could be used for this purpose. To extend the profile into the core, we incorporate data from the zero-order image of a *Chandra* High Energy Transmission Grating (HETG) observation of Her X-1 in its low state. Since the grating could affect the PSF shape, it would be better to use

non-grating observations, but there are very few appropriate observations available. Her X-1 has been observed a number of times with the gratings, but obsid 2749 is the only grating observation so far using Timed Event mode and thus suitable for constructing radial profiles. Obsid 2749 is a 50 ks GO "Target of Opportunity" observation taken on May 5, 2002. The radiation environment was quiescent. The zero order image was $\sim 8''$ off-axis, and the frame time was 3.2 s (see Table 1).

In Fig. 1, part of the derolled image of the Her X-1 obsid 3662 observation is plotted, with the ACIS transfer streak and the strut shadows indicated. The strut shadows are caused by the mirror support struts. The presence of these shadows indicates that the diffuse halo is predominantly caused by (in-plane) mirror scattering rather than a diffuse astrophysical halo due to dust scattering along the line of sight. The image of a diffuse astrophysical halo would be the superposition of many images like Fig. 1 which would tend to fill in the shadows. A portion of the azimuthal profile (1–2 keV, $1'$–$2'$ from the source, $1^\circ$ bins in azimuth $\phi$) is shown in right panel of Fig. 1. The depth of the shadows indicate that any cosmic dust halo contribution cannot be more than $\sim 1/4$ of the observed halo, confirming that the diffuse halo is primarily caused by mirror scattering.

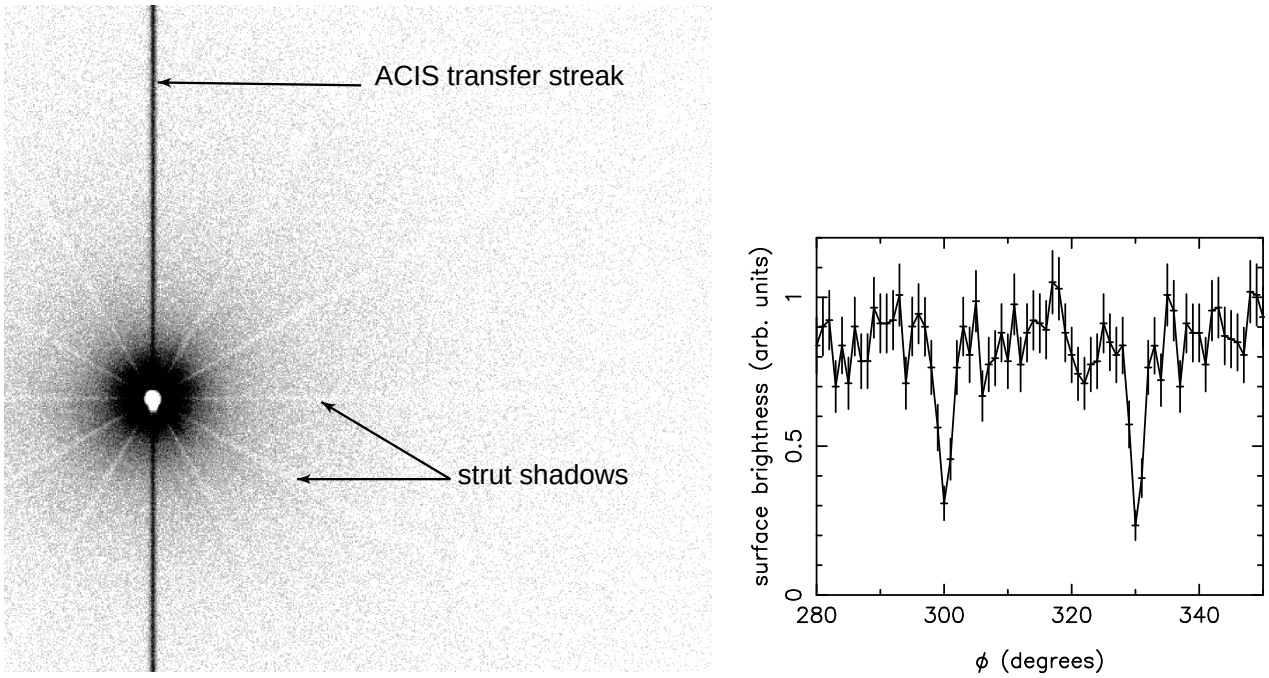


**Figure 1.** Left: Schematic of the deep Her X-1 wings observation. The ACIS transfer streak results from photons hitting the detector during the frame transfer to the frame store. The observation is notable for showing the shadows produced by the mirror support struts. Right: azimuthal variation of the 0.5–2.0 keV diffuse emission 1–$2'$ from the source. The $\phi$–binning was $1^\circ$.

## 3. PILEUP

The determination of pileup is important for understanding these observations. For observations of the core and inner wings, we need to know that the core really is unpiled. For the deep PSF wings observation, we need to know how far into the core the profile can be extended before pileup becomes an issue. In order to assess the degree of pileup, we use modified versions of diagnostics used in [4].

The first approach is a crude estimate based on Poisson statistics. For the diffuse scattered emission, we estimate the source rate such that there is a 5% probability that two events will land in a $3 \times 3$ pixel island within a single frame (3.1 s for obsid 3662). This is only approximate, since the diffuse emission is not uniform. Because the scale of the central core of the PSF is sub-pixel, for the core we estimate the rate such that there

is a 5% probability that two events will land in a single pixel within a frame (3.2 s for obsid 2749). In the top panels of Fig. 2, the radial profiles are plotted and the Poisson-based pileup estimate is indicated as a horizontal line. The top left panel shows the deep wings observation; we estimate that pileup is becoming significant $\sim 8''$ from the source. Moving radially inward, the profile peaks, then plummets to zero as pileup becomes extreme and all events are morphed into bad events. The top right panel shows the corresponding estimate for the Her X-1 zero-order image. In this case, there might be marginal pileup in the core.

Grade migration provides another pileup diagnostic [4]. Pileup tends to manifest as a migration of grades, *e.g.*, from grade 0 to other grades; the fraction of grade 0 events decreases, and the fraction of grade 6 events increases. If the pileup is severe enough, all grades migrate to grade 7, a bad grade, and are filtered out. Sufficiently bad grade migration removes events from the telemetry stream altogether. In the core of the Her X-1 image, the events have all migrated to bad grades, leaving a distinctive hole in the center.

Grade migration for a source imaged on the ACIS I array was examined in [4]; the behavior of the ratio of *ASCA* grade 0 to the sum of *ASCA* good grades (0, 2, 3, 4, 6), and the corresponding ratio for grade 6 seemed to provide a good diagnostic. The decrease of the grade 0 fraction and the the increase in the grade 6 fraction toward the core of the image was taken as an indication of pileup; the grade fractions became asymptotically flat at large radii.

The Her X-1 obsid 3662 images the source on the back-illuminated chip ACIS-S3. We examined the grade fractions as a function of radius, and found that the grade 6 fraction decreases radially outward, reaches a minimum, then increases. Similarly, the grade 0 fraction increases, reaches a maximum, then decreases. In order to understand this puzzling behavior, we examined grade ratios as a function of energy, and also examined grade ratios for background datasets. We found that the particle background has a significantly larger fraction of grade 6 events, particularly above $\sim 2$ keV. The peculiarity in the grade ratio profiles noted above was a result of the increasing importance of background events with increasing radius.

A cleaner evaluation of the diagnostic can be obtained by making use of the strong energy dependence of the grade ratios in the particle background. The spectrum of Her X-1 is soft, with most of the emission below $\sim 1$ keV. For moderate pileup, most of the detected piled up events will have energies less than $\sim 2$ keV. Thus, evaluating the radial profile for the grade fractions for energies between 0.5 and 2 keV emphasizes the grade migration of X-ray events, while reducing the contamination from grade 6 events in the background at higher energies. The grade ratio diagnostics are plotted in the bottom panels of Fig. 2. The left panel shows the grade ratio profiles for the deep wings observation, and the right panel shows the profile for the zero-order grating observation. For clarity, only the ratios for *ASCA* grades 0 and 6 are plotted. (In each case, these are fractions in grade 0 or grade 6 relative to the sum of the *ASCA* good grades 0, 2, 3, 4, and 6.) In the deep Her X-1 observation, the profiles are relatively flat at large radii, but inward of $\sim 7$ or $8''$, the grade 0 fraction declines, and the grade 6 fraction increases precipitously as pileup sets in. We thus estimate that pileup is a significant factor inside $\sim 8''$. For the zero-order data, the statistics are considerably worse; the indications are that the source is unpiled, with perhaps marginal pileup in the core.

## 4. DATA REDUCTION

In each case, the data were reprocessed without pixel randomization, starting with the level 1 event lists. In this initial analysis, we consider ACIS-S3 data only. Very Faint filtering is not applied at this time, but will be the subject of future investigation.

The effective area of the telescope is calculated for a large region centered on the specular image and thus includes scattered photons. Because a scattered photon travels a different path through the system than a specularly reflected photon, vignetting evaluated for the detected position is inappropriate. Instead, we apply the vignetting appropriate to the specular image. However, the detector Quantum Efficiency (QE), should be that appropriate to where the scattered photon was detected. The analysis thus requires somewhat unusual treatment of vignetting.

Ultimately, extracting the PSF is a combined spatial/spectral problem: one wants the spatial profile of the wings as a function of energy. Unfortunately, there do not currently exist tools to deal easily with a combined spatial/spectral analysis. Spectra can be extracted for narrow annuli, but there is presently no straightforward

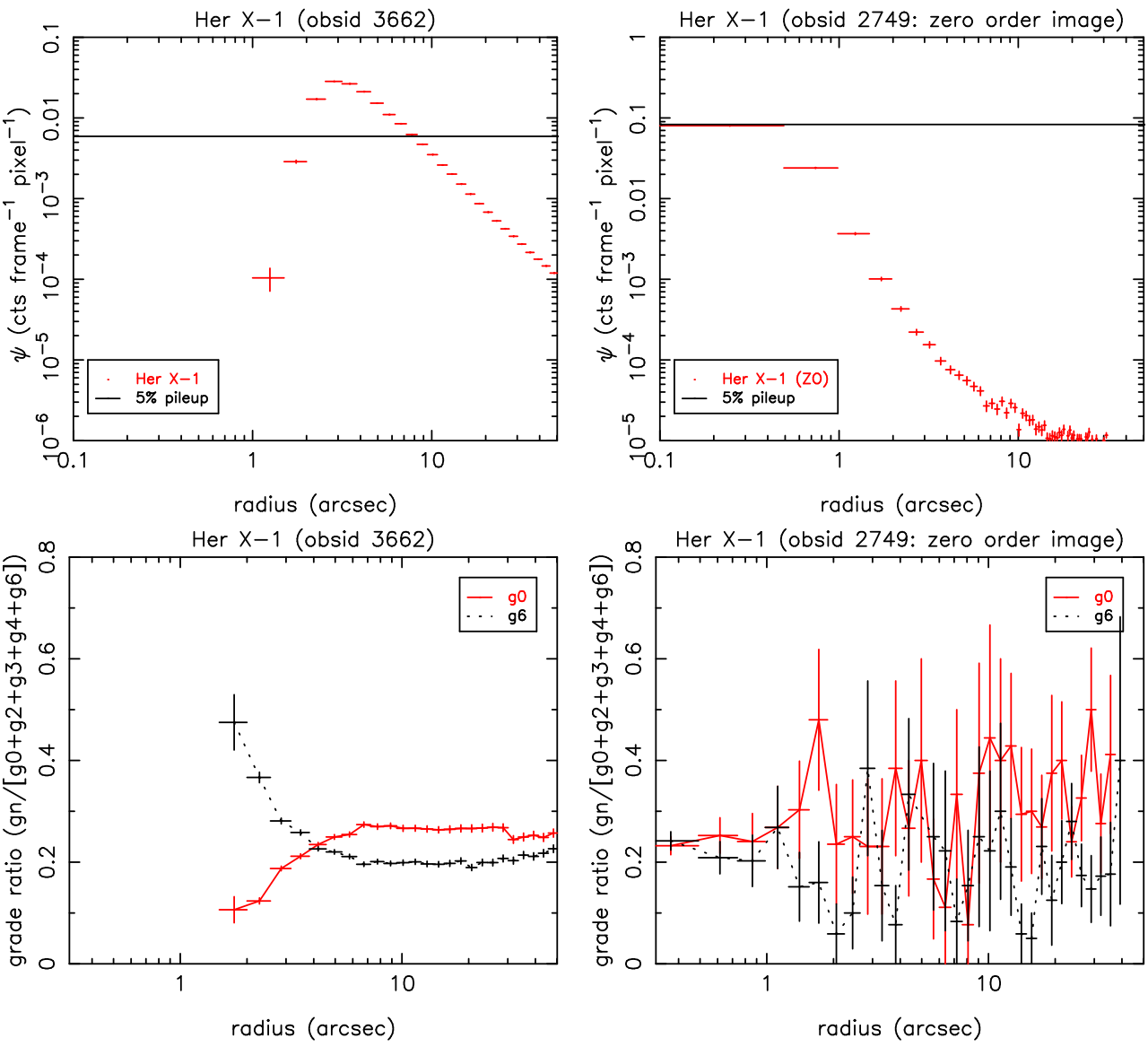


**Figure 2.** Top left: Her X-1 obsid 3662 surface brightness profile; the horizontal line indicates an estimate of the rate at which pileup is $\sim 5\%$. Top right: Her X-1 obsid 2749 surface brightness profile; the horizontal line indicates an estimate of the rate at which pileup is $\sim 5\%$. Bottom right: Profiles of the ratios of grades 0, 2, 3, 4, and 6 to the sum of grades 0, 2, 3, 4, and 6 for obsid 3662. Bottom right: Profiles of the ratios of grades 0, 2, 3, 4, and 6 to the sum of grades 0, 2, 3, 4, and 6 for obsid 2749.

way to apply an on-axis effective area and off-axis detector QE. Alternatively, data could be binned into images, but it is not straightforward to account for the spectral variation. An overall spectrum can be used for weighting the image, but the spatial distribution of mirror scattering is a function of energy.

The approach we have taken is to construct narrow-band count images for the deep wings observation (obsid 3662). The bands are $\Delta E = 0.1$ keV for 0.4–2.2 keV, $\Delta E = 0.2$ keV for 2.2–8.0 keV, and $\Delta E = 0.5$ keV for 8.0–10.0 keV. For the same energy bins, dithered QE maps were constructed using the *CIAO** tools `mkinstmap` to construct the QE map, and `mkexpmap` to project the QE map to the sky, including the effects of dither, but

**CIAO* is a set of analysis tools produced by the *Chandra* X-ray Center. See `http://cxc.harvard.edu/ciao/`.

excluding the HRMA effective area. Instead, the mirror effective area was evaluated separately for a small ($10''$ radius) region centered on the position of the specularly imaged source. Exposure-corrected images were then formed by dividing the counts images by the dithered QE maps, the total exposure time, the effective area at the source position, and a correction for the low-energy QE degradation. For the Her X-1 zero-order data (obsid 2749), the statistics were considerably poorer, so we used $\Delta E = 1.0$ keV bins for 1.0–8.0 keV.

For obsid 3662, the effect of background was evaluated using the appropriate blank sky background data (acis7sD20001201bkgrndN002.fits) obtained from the *Chandra* calibration database[†]. The sky background dataset was reprojected to the sky using the obsid 3662 aspect solution. Narrow-band counts and dithered QE maps were constructed, and exposure-corrected images were constructed. As noted in §2 the radiation environment was quiescent; based on comparing the rates for 11–13 keV, the background dataset was scaled by 1.0483. In order to match the coarser energy binning of the zero-order data (see below), the finely binned counts, QE, and exposure-corrected images were also summed to produce $\Delta E = 1.0$ keV images.

The zero-order data were handled somewhat differently. Because of the limited statistics, coarser 1 keV energy bins were used. The spectrum was extracted for a $10''$ radius region centered on the source, and for background regions on either side of the source. An approximate spectral weighting was constructed from the background subtracted spectrum (divided by the ARF) and used in weighting the QE maps. In addition, the image binning was 1/4 pixel in both directions to minimize pixelization errors in evaluating the profiles.

Radial profiles were extracted using annular regions centered on the source; the radial binning was variable. The inner bins were defined as $\theta_i = \theta_{i-1} + \Delta\theta$. Beyond a given radius ($2''$ for obsid 2749, $20''$ for obsid 3662), the radii increased faster than linearly with $\theta_i = 1.1 \times \theta_{i-1}$. Asymptotically, this provides approximately logarithmic binning. For logarithmic binning, a powerlaw $\propto \theta^{-2}$ would produce approximately the same number of source counts in each bin. Extraneous sources were excised from the annular regions, and the regions were also clipped near chip boundaries (allowing for the extent of the dither pattern). The ACIS transfer streak for the bright central source significantly contaminates the profile at large $\theta$. For obsid 3662, a narrow (10 pixel) rectangle centered on the streak was therefore excised. For obsid 2749, removing the transfer streak was not deemed necessary (the streak contamination remains relatively small for the range of $\theta$ of interest); however, to avoid potential contamination from the dispersed spectra, narrow rectangular exclusion regions (not obscuring the core region) were applied.

For each energy band, radial surface brightness profiles were constructed from the counts image and the QE and exposure corrected image; the counts image data were used to propagate errors for the QE and exposure-corrected data. This results in surface brightness profiles for the quantity

$$\langle \psi_i \rangle_{\Delta\theta} = \frac{1}{A_{eff}\, t_{exp}\, q} \langle C_{corr,i} \rangle_{\Delta\theta} \tag{1}$$

where $C_{corr} = C_{counts}/QE$ is the QE-corrected counts image and $C_{corr,i}$ is value of $C_{corr}$ averaged over annulus $i$ with width $\Delta\theta$. $A_{eff}$ is the effective area at the source position, $t_{exp}$ is the exposure time, and $q$ is a correction factor for the low-energy QE degradation at the time of the observation (very close to 1 for $E \gtrsim 1$). The $\langle\rangle_{\Delta\theta}$ indicates an average over the corresponding annulus of width $\Delta\theta$.

## 5. ANALYSIS

The first stage of the analysis was to fit powerlaw profiles to the radial profiles extracted for the narrow-band Her X-1 wings data. These were simultaneous fits to a powerlaw plus constant background to both the Her X-1 dataset and the corresponding blank sky background dataset; the powerlaw amplitude was frozen at 0 in the background dataset fits. The resulting profiles are steep at low energies, rapidly becoming shallower toward $\sim 1.8$ keV. Below $\sim 1$ keV, the low-energy QE degradation is very important; an approximate correction has been applied, but the magnitude and spatial nonuniformity of the effect are still under investigation. Consequently, the derived powerlaw indices for $E \lesssim 1$ keV are somewhat uncertain. The powerlaw slope is fairly constant for $\sim 1.8$–5.0 keV, and steepens again above $\sim 5$ keV. The steepening above 5 keV is likely the result of the roughest mirror pair (MP1) dropping out as its effective area rapidly declines with increasing energy.

[†]http://cxc.harvard.edu/caldb/

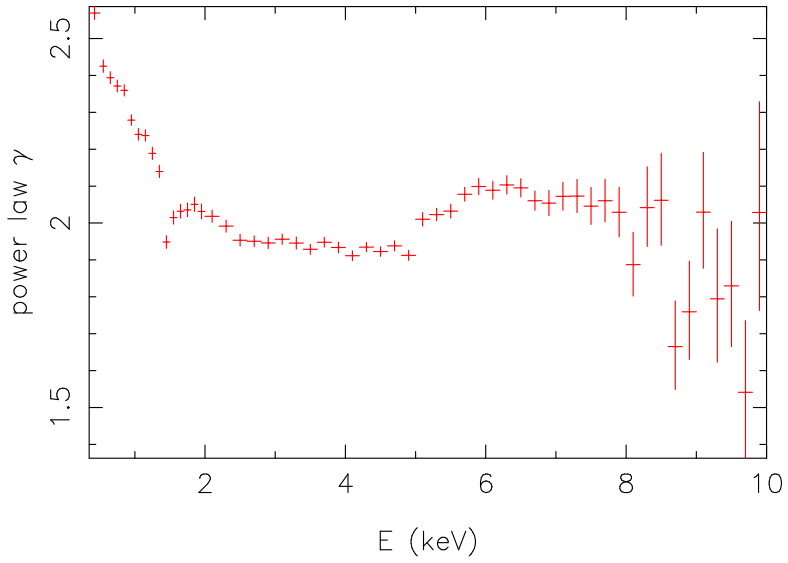


**Figure 3.** Powerlaw index for fits to the narrow band obsid 3662 data.

The glitch at 1.5 keV deserves comment. There is no reason why the profile slope should be discontinuous at that energy. A possible explanation was revealed by examination of spectra of diffuse emission extracted from annular regions centered on the source. For radii beyond $\sim 2'$, the spectra show a pronounced line feature just below 1.5 keV (see Fig. 4, left panel). This is not a feature in the Her X-1 spectrum — it does not appear in the transfer streak spectrum (see Fig. 4, right panel). We believe this to be an artifact, since it is not evident in the sky background data, nor in the Her X-1 transfer streak data. Based on energy, it is tentatively identified as an Al K$\alpha$ fluorescence feature, but there is no obvious source for the emission. The aluminum support struts in the central aperture plate are illuminated by Her X-1 and are in the view of the focal plane but the very small solid angle subtended by the detectors would seem to make this unlikely. Similarly, there is some aluminum in the optical blocking filter which is closer to the detector, but the aluminum is very thin (only $\sim 1300$ Å) so again it seems unlikely given the small optical depth and low fluorescent yield of aluminum. For now, we exclude the 1.4-1.6 keV band from the analysis of the obsid 3662 data and interpolate from the neighboring bands.

The normalization of the wing profiles is problematic. Ideally one would normalize to the total power contained within a fiducial radius. For the deep observation of the wings (obsid 3662) the core is very heavily piled up and most of the counts from the source are lost to grade migration into bad events. In order to try to apply a consistent normalization (so that the wings at different energies can be compared), we merge multiple datasets: a Her X-1 zero-order image with minimal pileup (obsid 2749), and the deep Her X-1 wings observation, which is heavily piled up in the core (obsid 3662). Our pileup estimator (§3) indicates that for obsid 3662 pileup is significant within $\sim 8''$. On the other hand, the grating zero-order image is very faint, and statistics are becoming problematic by $\sim 10''$ from the core. A longer core observation (or a stack of observations) would help reduce the uncertainties, as would slightly piled observations providing data for the near wings at the few arcsec to 10's of arcsec range.

We proceed by performing a simultaneous fit to the profiles using the fit function:

$$f(\theta) = \frac{A_0}{\left[1 + \left(\frac{\theta}{\theta_0}\right)^2\right]^{\gamma/2}} + A_1 \exp\left[-4\ln(2)\left(\frac{\theta}{\theta_1}\right)^2\right] + A_2 \exp\left[-4\ln(2)\left(\frac{\theta}{\theta_2}\right)^2\right] + B \qquad (2)$$

where $\theta_1$ and $\theta_2$ are the Gaussian full widths at half maximum (FWHM's), and $\theta$ is the angle from the specular image. A modified Lorentzian is used to account for the far wings; to avoid problems with the scale length

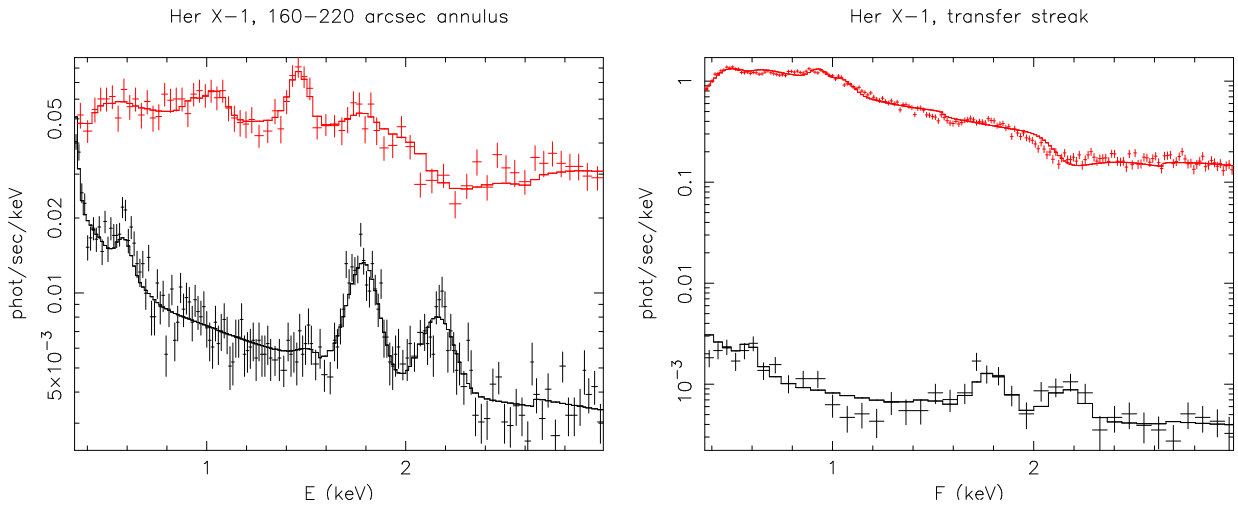


**Figure 4.** Left: Spectrum for Her X-1 (obsid 3662) for an annular region 160–220″ from the source. Right: Spectrum for the transfer streak of Her X-1 (obsid 3662). Frame transfer is effectively a different ACIS mode, and it has not been calibrated. There is a shift in the slope of the gain of at least a few percent; this can be seen clearly at the Ir M edge just above 2 keV. (The rate has not been corrected for the effective transfer streak duty cycle.) In both panels, the upper curve is the Her X-1 obsid 3662 data. The lower curve shows the spectra for the corresponding blank sky data.

reaching unrealistically small values, $\theta_0$ was frozen at 1″. The profile approaches the powerlaw $A_0/(\theta/\theta_0)^\gamma$ at large $\theta$. The first Gaussian, with FWHM $\theta_1 \sim 0.75''$, models the core. The second Gaussian models possible structure at scales of $\theta_2 \sim 1''$–$2''$. Finally, the constant term models the background. Simultaneous fits were performed to the Her X-1 obsid 3662 profile, the corresponding blank sky background (with $A_0$, $A_1$, and $A_2$ frozen at 0), and the Her X-1 obsid 2749 zero-order profile. The Her X-1 datasets were then renormalized using the integral of the fit function from 0–5′, and the rescaled profiles combined. The results for 1.0–2.0 keV and 3.0–4.0 keV are displayed in Fig. 5, and those for 5.0-6.0 keV and 7.0-8.0 keV are displayed in Fig. 6. The corresponding model parameters are given in Table 2. The errors are purely statistical and based on 90% confidence intervals in the fits. The error in the modified Lorenztian amplitude was estimated by adding (in quadrature) an error based on the mean relative error for bins in the overlap region from 8″ to 20″. None of the errors include systematic errors such as possible broadening of the zero-order image by scattering from the gratings. Finally, note that there are suggestions that further components may be needed in the $\sim$ 2–10″ range; the model function underpredicts $\sim$ 2–4″ in the $\Delta E = 3.0$–4.0 plot.

**Table 2.** Model Parameters

| $\Delta E$ | $A_0^\dagger$ | $\gamma$ | $A_1$ | $\theta_1$ | $A_2$ | $\theta_2$ |
|---|---|---|---|---|---|---|
| 1.0–2.0 | $0.00708 \pm 0.00585$ | $2.110 \pm 0.009$ | $0.782 \pm 0.175$ | $0.732 \pm 0.016$ | $0.111 \pm 0.025$ | $1.634 \pm 0.042$ |
| 3.0–4.0 | $0.00661 \pm 0.00366$ | $1.925 \pm 0.005$ | $0.692 \pm 0.125$ | $0.787 \pm 0.019$ | $0.052 \pm 0.009$ | $1.926 \pm 0.114$ |
| 5.0–6.0 | $0.00908 \pm 0.00479$ | $2.005 \pm 0.006$ | $0.642 \pm 0.097$ | $0.619 \pm 0.037$ | $0.157 \pm 0.024$ | $1.500 \pm 0.035$ |
| 7.0–8.0 | $0.00807 \pm 0.00663$ | $2.023 \pm 0.017$ | $0.603 \pm 0.154$ | $0.756 \pm 0.044$ | $0.133 \pm 0.034$ | $1.500 \pm 0.073$ |

$^\dagger$estimated error includes scaling uncertainties

A comparison with an Ar Lac profile obtained from an HRC-I observation indicates that the Her X-1 zero-order profile is broader than the HRC-I profile, with the amplitude at 10″ several times higher than for the Ar Lac profile. The source of this discrepency is under investigation. It is uncertain at this point whether this is a detector pixelization effect; possibly scattering by the gratings is broadening the zero-order image profile.

## 6. SUMMARY AND CONCLUSIONS

We have analyzed a deep exposure of Her X-1 which was obtained to probe the wings of the *Chandra* PSF to large angles. This is a superb dataset which allows examination of the wings with fine spectral and spatial resolution (averaged over azimuth). One concern in using an astrophysical source such as Her X-1 as a PSF wings calibration object is that X-ray scattering by cosmic dust along the line of sight could bias the PSF determination. The presence of deep mirror support strut shadows in the image data indicates that any such dust halo contribution is at worst $\lesssim 25\%$ for $E \geq 1$ keV.

The powerlaw slope at large angles shows a significant glitch around 1.5 keV, and spectra extracted from broad annuli beyond $\sim 2'$ show a prominent spectral line feature at an energy possibly consistent with being an Al K$\alpha$ line. The line feature does not appear in the extracted ACIS transfer streak spectrum for Her X-1, and does not appear in blank sky background fields. It thus appears to be an artifact due to the extremely bright X-ray source, although we are presently unable to account for its origins. Data for 1.4–1.6 keV are excluded from the subsequent analysis.

Because an extremely bright source is required in order to observe the wings above background, the core and near wings are lost or heavily affected by ACIS pileup. We examined several approaches to assessing pileup, and conclude that the wings observation shows significant pileup within $\sim 8''$ of the specular image.

The normalization of the PSF wings has been problematic, since the extreme pileup in the core results in loss of most of the X-rays imaged from the source. Previous efforts at normalization have used spectra extracted from the ACIS transfer streak. However, frame transfer is in essence a separate ACIS mode, and very little work has been done in calibrating detector properties during the frame transfer. The detector gain is somewhat different during frame transfer than during frame accumulation; this can be seen in the mismatch at the Ir M edge just above 2 keV (Fig. 4). Heinke *et al.* [5] estimate a change in the gain slope of $\sim 7\%$; our estimates based on the Her X-1 dataset indicate $\sim$ 2–3%.

In order to normalize the wing profiles, we tried a different approach here — utilizing datasets with smaller pileup to probe into the core of the PSF. We used the zero-order grating data for an observation of Her X-1 in the low state to sample the core and inner wings of the PSF; the indications are that the zero-order is not significantly piled up. These data were combined with the deep wings observation to produce profiles extending from the core out to the wings, providing a normalization for the wings. Unfortunately, this normalization remains somewhat uncertain. The faintness of the zero-order Her X-1 image means that the statistics degrade rapidly with $\theta$, producing relatively large uncertainties beyond $\sim 8''$ where the profile overlaps with the deep wings observation. Furthermore, comparison with an HRC-I observation of Ar Lac indicates that the zero-order Her X-1 image is more extended than Ar Lac; the cause for this is under investigation, In addition, presence of the grating in the optical path introduces additional complications such as potential scattering from the gratings. These issues can be addressed by searching for additional observations deep enough to examine the near wings at $\sim$ 5–20$''$ (or a stack of shorter observations). This will be necessary in any event, since the ultimate aim is to characterize the PSF as a function of energy from the central core, through the near wings, out to large radii.

Both approaches to obtaining the normalization (transfer streak spectrum and profile matching) have problems; at this point, the uncertainties in the transfer streak estimate are probably smaller.

## ACKNOWLEDGMENTS

This work was supported by NASA Contract NAS8-39073.

## REFERENCES

1. L. P. van Speybroeck, D. Jerius, R. J. Edgar, T. J. Gaetz, P. Zhao, and P. B. Reid, "Performance expectation versus reality," in *Proc. SPIE Vol. 3113, p. 89-104, Grazing Incidence and Multilayer X-Ray Optical Systems, Richard B. Hoover; Arthur B. Walker; Eds.*, pp. 89–104, July 1997.
2. Q. Z. Liu, J. van Paradijs, and E. P. J. van den Heuvel, "A catalogue of high-mass X-ray binaries," *Astron. Astrophys. Suppl.* **147**, pp. 25–49, Nov. 2000.
3. J. M. Dickey and F. J. Lockman, "H I in the Galaxy," *Ann. Rev. Astron. Astrophys.* **28**, pp. 215–261, 1990.

4. R. K. Smith, R. J. Edgar, and R. A. Shafer, "The X-Ray halo of GX 13+1," *Astrophys. J.* **581**, pp. 562–569, Dec. 2002.
5. C. O. Heinke, P. D. Edmonds, J. E. Grindlay, D. A. Lloyd, H. N. Cohn, and P. M. Lugger, "A Chandra X-Ray study of the dense globular cluster Terzan 5," *Astrophys. J.* **590**, pp. 809–821, June 2003.

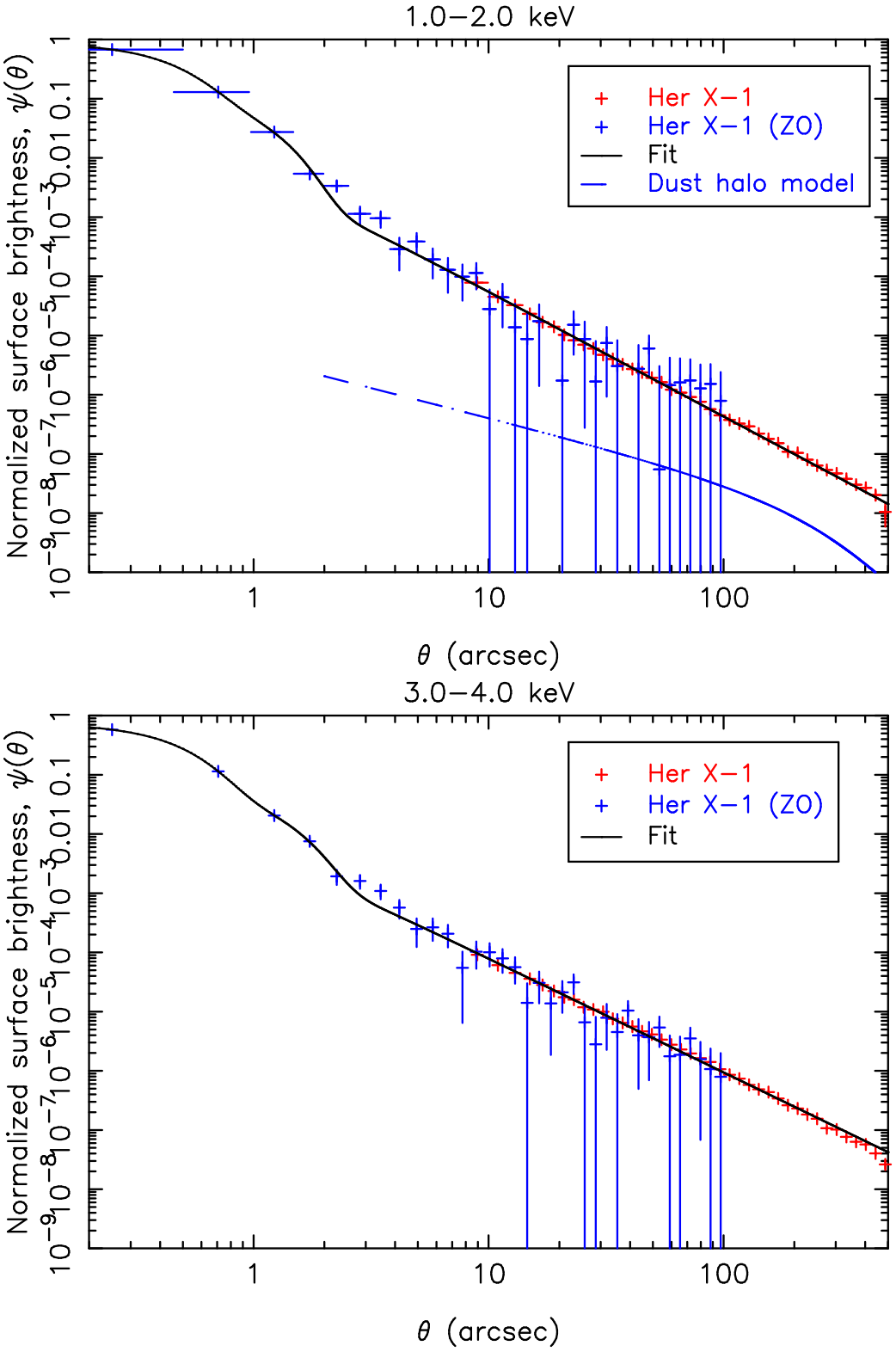


**Figure 5.** Profiles for the *Chandra* wings. Top panel: 1.0–2.0 keV. The cosmic dust halo profile for a column of $N_H = 1.8 \times 10^{20}$; this profile is included for comparison only and is not part of the fit. The error bars are purely statistical and do not include the errors from renormalizing the datasets. Bottom panel: 3.0–4.0 keV.

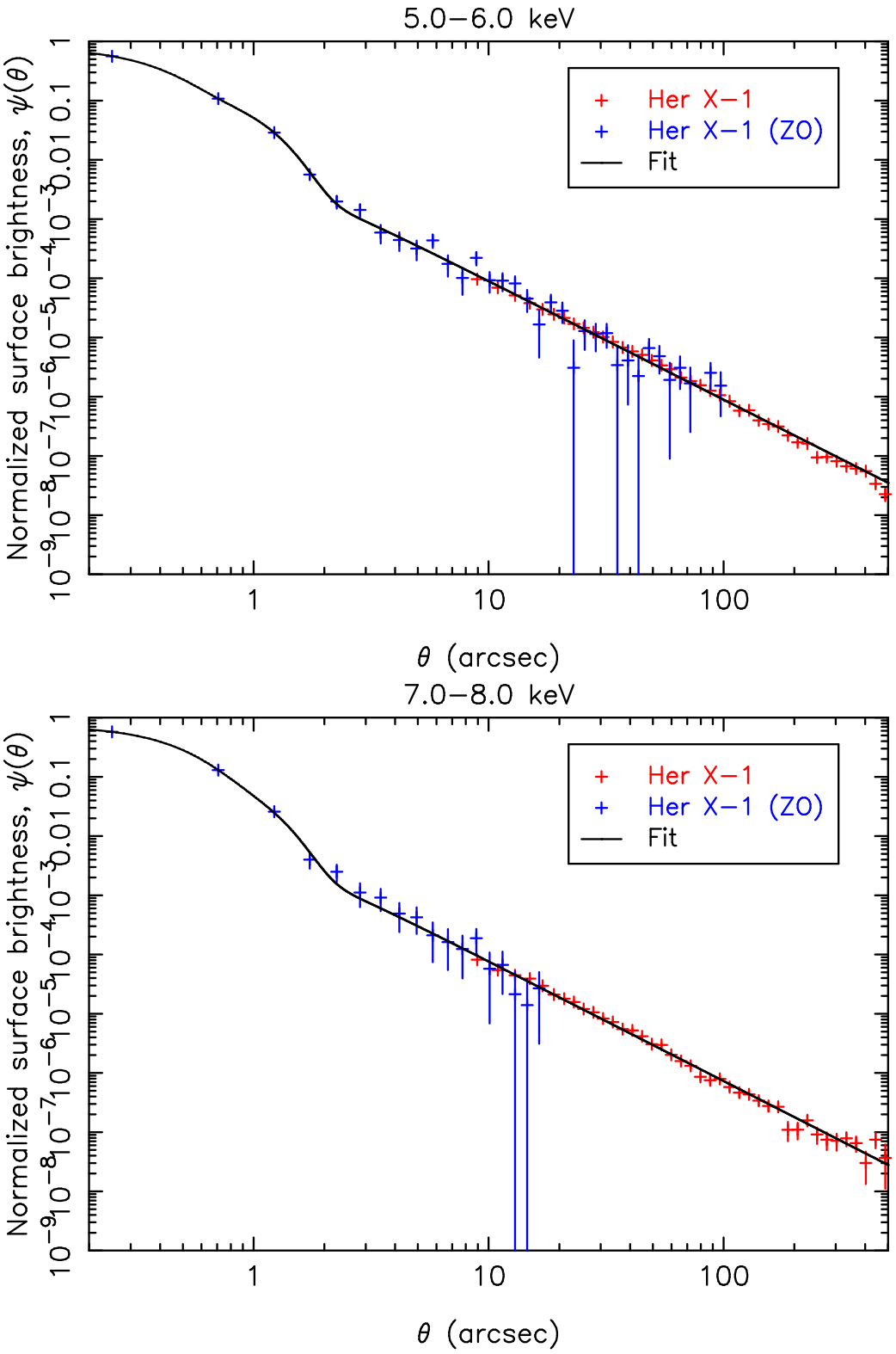


**Figure 6.** Profiles for the *Chandra* wings. Middle panel: 5.0–6.0 keV. Bottom panel: 7.0–8.0 keV. (See Fig. 5).